

Scaling Sim-to-Real Reinforcement Learning for Robot VLAs with Generative 3D Worlds

Andrew Choi¹, Xinjie Wang¹, Zhizhong Su¹, and Wei Xu^{1,†}
 {firstname.lastname}@horizon.auto
¹Horizon Robotics [†]Corresponding author



Figure 1: Overall pipeline diagram. Real-world data trains an imitation policy π_{pre} . Task descriptions are fed to a language-driven scene designer, which forwards layouts to a 3D world generative model to produce digital twin scenes. π_{θ} is trained across these scenes, initialized from π_{pre} , with massive parallelization and domain randomization. Finally, the trained π_{θ} is deployed in the real world.

Abstract: The strong performance of large vision–language models (VLMs) trained with reinforcement learning (RL) has motivated similar approaches for fine-tuning vision–language–action (VLA) models in robotics. Many recent works fine-tune VLAs directly in the real world to avoid addressing the sim-to-real gap. While real-world RL circumvents sim-to-real issues, it inherently limits the generality of the resulting VLA, as scaling scene and object diversity in the physical world is prohibitively difficult. This leads to the paradoxical outcome of transforming a broadly pretrained model into an overfitted, scene-specific policy. Training in simulation can instead provide access to diverse scenes, but designing those scenes is also costly. In this work, we show that VLAs can be RL fine-tuned without sacrificing generality and with reduced labor by leveraging 3D world generative models. Using these models together with a language-driven scene designer, we generate hundreds of diverse interactive scenes containing unique objects and backgrounds, enabling scalable and highly parallel policy learning. Starting from a pretrained imitation baseline, our approach increases simulation success from 9.7% to 79.8% while achieving a $1.25\times$ speedup in task completion time. We further demonstrate successful sim-to-real transfer enabled by the quality of the generated digital twins together with domain randomization, improving real-world success from 21.7% to 75% and achieving a $1.13\times$ speedup. Finally, we further highlight the benefits of leveraging the effectively unlimited data from 3D world generative models through an ablation study showing that increasing scene diversity directly improves zero-shot generalization.

Keywords: sim-to-real reinforcement learning, vision-language-action models, robot manipulation, generative simulation

1 Introduction

Though internet-scale training of VLMs has seen explosive success, the performance of VLAs has comparatively lagged behind. As of recently, the dominant pipeline for training robot foundation models consists of leveraging all layers of the “data pyramid”: 1) pretraining a VLM backbone on internet-scale data, 2) further pretraining via imitation learning on large-scale robot datasets [1, 2], and 3) task- and embodiment-specific fine-tuning via imitation learning, real-world reinforcement learning, or sim-to-real reinforcement learning. While the first two stages are largely addressed by training on publicly available data, the third stage often requires significant human involvement.

For imitation learning and offline RL, this involvement comes in the form of manual real-world data collection. For real-world RL, human-in-the-loop (HIL) supervision is often required to achieve sufficient sample efficiency [3, 4]. Conversely, sim-to-real RL eliminates the need for manual data collection and HIL by instead generating an abundance of data through massive parallelization [5], but introduces new challenges in the form of visual and dynamic sim-to-real gaps. Furthermore, though elements of the learning pipeline such as environmental resets and reward detection are significantly easier in simulation, designing the 3D environments themselves—albeit a one-time cost—also requires substantial human effort.

An often-overlooked drawback of real-world fine-tuning is the loss of generality that arises when training on only a small number of scenes. Because scaling scene diversity in the physical world is prohibitively expensive, most prior work fine-tunes VLAs in narrowly scoped settings. As a result, fine-tuning frequently transforms a broadly pretrained VLA into an overfitted, scene-specific policy. In this paper, we show that generative 3D world models can automatically construct large training distributions of interactive environments for RL fine-tuning of VLAs, enabling scalable sim-to-real learning beyond the small number of hand-designed environments used in prior work. A snapshot of the overall pipeline can be seen in Fig. 1. Overall, our main contributions involve showing that

- 1. Reinforcement learning and 3D world generative models strongly complement the large capacity of VLAs.** We introduce a language-driven scene designer that converts task descriptions into structured scene layouts, which are then used by a 3D world generative model to produce fully interactive environments. Paired with highly parallelized RL, this enables VLAs to be fine-tuned across a wide variety of scenes without requiring manual scene design. In this work, we fine-tune a pretrained VLA in simulation, achieving a **70.1-percentage-point improvement in success rate and a 1.25× task completion speedup** across 100 unique generated scenes.
- 2. Increasing scene diversity substantially improves zero-shot generalization.** Through extensive ablations in simulation, we show that zero-shot generalization scales positively with training distribution diversity. Results show that fine-tuning on 50 scenes can **increase zero-shot success rate by 24.8 percentage points** compared to fine-tuning on a single scene.
- 3. Techniques for sim-to-real transfer of shallow models carry over to VLAs.** We achieve positive sim-to-real deployment results by leveraging 1) the digital twin-like quality of the generated 3D objects and scenes, 2) simple domain randomization, and 3) using PD control with gravity compensation. We achieve a **53.3-percentage-point improvement in success rate and a 1.13× task completion speedup** across 12 scenes and 240 real-world experiments.
- 4. RL fine-tuning flow matching VLAs into Gaussian policies is effective.** We demonstrate that PPOFlow—a PPO-based [6] variant of ReinFlow [7]—effectively fine-tunes large pretrained flow matching VLAs. PPOFlow can transform a multi-step flow matching policy into a single-step Gaussian policy, which was previously thought to harm performance [8]. Instead, our findings directly support the recent work of Pan et al. [9] in that the multimodality of diffusion models is not an important factor for having a high-performing robot policy. Furthermore, we demonstrate an **inference latency speedup of 2.36×** through PPOFlow by removing the need for iterative denoising of actions, similar to consistency policies [10, 11, 3]. More details can be seen in Sec. B.

2 Related Work

VLA models. Motivated by the successes of VLMs in computer vision and NLP, large open-source robot datasets, both physical [12, 1] and synthetic [2, 13], have been created to facilitate supervised pretraining of VLAs. Using such datasets, a series of open-source robot VLAs have been released, such as OpenVLA [14], SpatialVLA [15], GraspVLA [2], π_0 [16], $\pi_{0.5}$ [17], and many more. A common strategy is to then supervised fine-tune a pretrained model with imitation learning on task-specific demonstration data [18]. Though straightforward, such approaches often suffer in performance when encountering out-of-distribution states [19] and recent work has suggested that dataset fragmentation introduces unwanted shortcut learning of VLAs [20]. Given this, there has been an increasing trend of instead using reinforcement learning to fine-tune VLAs.

Learning in real. One popular strategy for RL fine-tuning VLAs has been to perform RL directly in the real world [3, 21, 4, 22, 23, 24, 25]. Though RL in real circumvents issues arising from sim-to-real gap, such methods must handle tedious issues that don't arise in simulation. One key consideration is how to administer the reward signal. For simplicity, most methods often rely on a sparse success reward signal, which is then administered by either a trained reward model [21, 23, 3, 26], human engineered checkers [24], or a human labeler [4]. Some approaches have used more dense reward formulations such as steps-to-go [22]. Another consideration is how to perform scene resets, which can be handled by manual resets [3, 4], scripted resets [3, 25], or learning the reset task [21, 23, 24]. Lastly, it has become increasingly evident that a combination of offline RL and human-in-the-loop learning is a key necessity to get reasonable sample efficiency when executing RL on real hardware [23, 3, 4]. Though such methods have shown impressive results for learning tasks on a set scene and objects in a reasonable amount of time, the ability to maintain the generality of such policies in both scene and object space through scaling is a major question, especially given the necessity for human guidance.

Learning in simulation. The other method of RL fine-tuning VLAs is to do so in simulation [27, 28, 5]. Compared to real, training in simulation offers numerous benefits, such as oracle success detection, automatic resets, and access to privileged information for teacher-student training setups [29, 30, 31, 32]. Due to the domain difference, special consideration must be taken to ensure that such policies transfer from sim-to-real successfully. Several strategies for handling the sim-to-real gap exist including domain randomization [29, 33], real-to-sim delta action models [34], real-to-sim physical property estimation [35], real-to-sim scene reconstruction [36, 31, 37], and more (albeit many of these methods have been used on smaller models, rather than foundation-scale). Training shallow models from scratch often requires heavily engineered reward functions [29, 34, 33]. With this, fine-tuning VLAs has immense benefits over shallow models as a well-trained VLA prior only requires a sparse reward and massive parallelization to learn [5]. Recent works for RL fine-tuning VLAs include leveraging real-to-sim-to-real robot video synthesis for leveraging both the real data and scalability of simulation [27] as well as learning within learned world models [28]. In contrast to these prior works, our main focus in this manuscript is to instead explore a different angle: can RL fine-tuning be done for as wide of a scene distribution as possible? And if so, how does increasing scene diversity improve zero-shot generalization?

3D world generative models. Constructing large-scale, realistic 3D simulation environments remains a fundamental bottleneck for sim-to-real reinforcement learning. Existing 3D generative paradigms (e.g., TRELLIS [38], WorldGen [39]) primarily focus on producing static visual assets that lack physical interactivity. Although recent works such as Holodeck [40] and RoboGen [41] attempt to procedurally construct interactive environments, end-to-end generation of task-level physical scenes remains challenging. Recently, emerging generative engines, exemplified by EmbodiedGen [42], have enabled natural language-driven generation of interactive 3D scenes. In this work, we explore the integration of generative 3D engines as a low-cost, highly parallelizable digital twin pipeline for scalable data generation, enabling large-scale RL fine-tuning of VLA models in simulation.

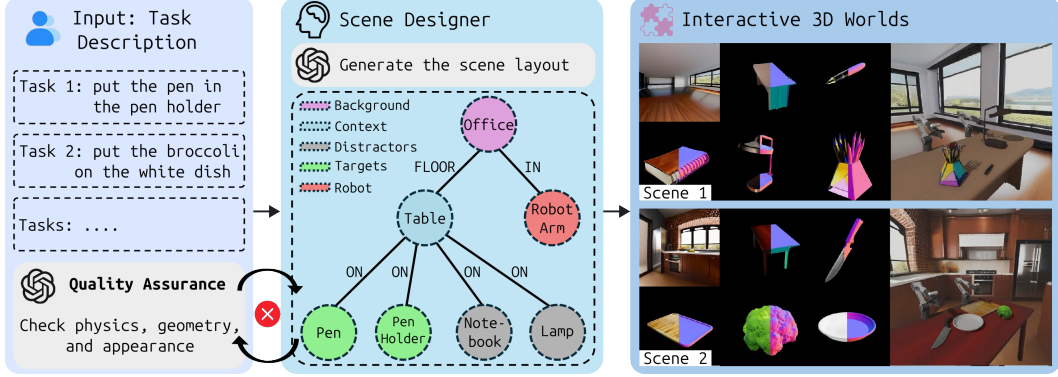


Figure 2: Overview of the simulation environment generation pipeline. A GPT-4o-powered scene designer converts task descriptions into structured scene graphs over semantic roles and spatial relations, which are instantiated into fully interactive 3D worlds. A quality assurance loop filters physically implausible configurations before simulation, enabling scalable, on-demand generation of diverse environments for RL training.

3 Methodology

Generative simulation. To construct large-scale, physically interactive 3D environments for sim-to-real reinforcement learning, we employ ManiSkill 3 [43] as our GPU-parallelized simulator and extend EmbodiedGen [42] into a comprehensive simulation environment generation backend. As illustrated in Fig. 2, EmbodiedGen takes a structured scene tree layout as input and produces a fully interactive physical 3D world via its text-to-3D asset generation and layout composition interfaces. We develop a scene designer powered by GPT-4o [44] that automatically produces valid scene layouts from task descriptions. Given an instruction such as “put the pen in the pen holder”, the scene designer parses it into a structured scene graph comprising core semantic roles (background, context, distractors, manipulation targets, and the robot) along with their spatial relations (e.g., ON, IN). This graph-based representation enables flexible, compositional control over scene complexity and distractor density, allowing systematic modulation of training difficulty. Each generated scene is then passed through an automated GPT-4o-driven quality assurance loop that checks physical plausibility and geometric consistency, discarding configurations that would cause simulation instability.

Markov decision process. We formulate our learning problem as a finite-horizon partially observable Markov decision process (POMDP) with state space \mathcal{S} , action space \mathcal{A} , and discount factor $\gamma \in [0, 1]$. At each timestep t , the agent receives an observation \mathbf{o}_t and selects an action \mathbf{a}_t according to a policy $\pi(\mathbf{a}_t | \mathbf{o}_t)$. An observation consists of an RGB image $\mathbf{I} \in \mathbb{R}^{H \times W \times 3}$, language instruction $\mathbf{e} \in \mathbb{R}^L$, and proprioceptive information in the form of end-effector pose $\mathbf{q} \in \mathbb{R}^7$, where L denotes the instruction length and \mathbf{q} is in (xyz, rpy, gripper) form. This full observation is given by $\mathbf{o}_t = [\mathbf{I}_t, \mathbf{e}_t, \mathbf{q}_t]$. Actions are represented as (end-effector delta-pose, binary gripper) action chunks $\mathbf{A} \in \mathbb{R}^{C \times 7}$, where C denotes the action chunk length. We treat each action chunk as a single decision step, resulting in a continuous action space $\mathcal{A} \subset \mathbb{R}^{C \times 7}$. The objective is to learn a policy that maximizes the expected discounted return $J(\pi) = \mathbb{E}_\pi \left[\sum_{t=0}^{T-1} \gamma^t r_t \right]$, where T denotes the episode horizon.

Flow matching models. For RL fine-tuning to work with solely a sparse reward signal, we look to use a pretrained robot foundation model to boost sample efficiency [5]. In this work, we use π_0 [16] as our baseline imitation model, initialized from a checkpoint pretrained on the BridgeV2 dataset [12]. The π_0 model is composed of a VLM backbone E_θ and an action expert head v_θ (left of Fig. 3). The π_0 model is trained using a rectified flow-matching objective

$$\mathcal{L}_{\text{flow}}(\theta) = \mathbb{E}_{\mathbf{o}_t, \mathbf{A}_t^1 \sim \mathcal{D}, \epsilon \sim \mathcal{N}(\mathbf{0}, \mathbf{I}), \tau \sim \mathcal{U}(0,1)} \left[\|v_\theta(\mathbf{A}_t^\tau, KV_\theta(\mathbf{o}_t), \tau) - (\mathbf{A}_t^1 - \epsilon)\|_2^2 \right], \quad (1)$$

where \mathcal{D} denotes the demonstration dataset, $\tau \in [0, 1]$ is the continuous integration time, $KV_\theta(\mathbf{o}_t)$ denotes the key-value tensors of $E_\theta(\mathbf{o}_t)$ for cross-attention, and $\mathbf{A}_t^\tau = \tau \mathbf{A}_t^1 + (1 - \tau)\epsilon$. Robot

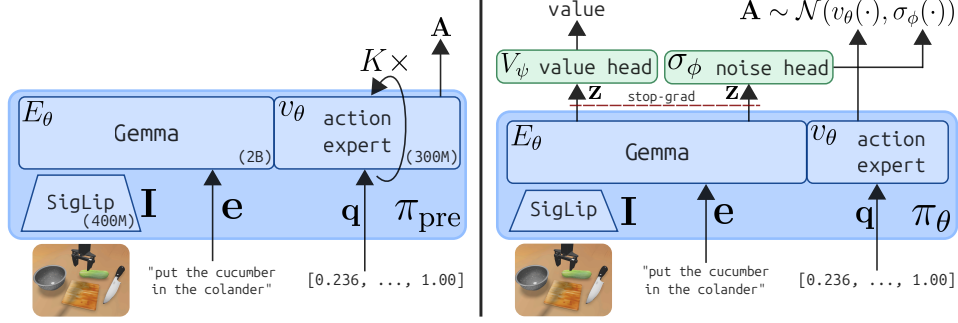


Figure 3: Architecture diagram of the π_0 model as a pretrained imitation model π_{pre} (left) and then modified for RL fine-tuning, π_θ (right).

actions are generated by numerically integrating the learned ODE

$$\frac{d\mathbf{A}_t^\tau}{d\tau} = v_\theta(\mathbf{A}_t^\tau, KV_\theta(\mathbf{o}_t), \tau), \quad (2)$$

where $\mathbf{A}_t^0 \sim \mathcal{N}(\mathbf{0}, \mathbf{I})$. We denote the resulting pretrained imitation policy as π_{pre} .

PPOFlow. As flow matching models are deterministic, the importance ratio cannot be computed, preventing standard PPO updates. ReinFlow solves this by injecting learnable noise $\sigma_\phi(\mathbf{A}_t^\tau, \mathbf{z}_t, \tau)$ into the numerical integration process, where \mathbf{z}_t denotes the stop-gradient hidden state $\mathbf{z}_t = \text{sg}(E_\theta(\mathbf{o}_t))$. This effectively converts each integration step $\mathbf{A}_t^{\tau+\Delta\tau} = \mathbf{A}_t^\tau + v_\theta(\mathbf{A}_t^\tau, KV_\theta(\mathbf{o}_t), \tau)\Delta\tau$ into a Gaussian sample

$$\mathbf{A} = \mathbf{A}_t^\tau + v_\theta(\mathbf{A}_t^\tau, KV_\theta(\mathbf{o}_t), \tau)\Delta\tau, \quad (3)$$

$$\mathbf{A}_t^{\tau+\Delta\tau} \sim \mathcal{N}(\mathbf{A}, \sigma_\phi(\mathbf{A}_t^\tau, \mathbf{z}_t, \tau)). \quad (4)$$

Let us denote the number of numerical integration steps as $K = 1/\Delta\tau$. This then allows us to compute the joint log probability of the denoising process for a particular step t as

$$\log \pi(\mathbf{A}_t^0, \dots, \mathbf{A}_t^1 | \mathbf{o}_t) = \log \mathcal{N}(\mathbf{0}, \mathbf{I}) + \sum_{k=0}^{K-1} \log \pi(\mathbf{A}_t^{(k+1)\Delta\tau} | \mathbf{A}_t^{k\Delta\tau}, \mathbf{o}_t), \quad (5)$$

where $K = 1/\Delta\tau$ is the number of integration steps. In addition to the noise head σ_ϕ , we also add a value head $V_\psi(\mathbf{z}_t)$ for estimating the state value. A full diagram of π_θ can be observed on the right side of Fig. 3. We can then directly use the log probability (Eq. 5) to compute the following power-scaled importance ratio, which is then used along with the value from V_ψ in the original PPO clipped objective

$$\hat{r}_t = \left(\frac{\pi_\theta(\mathbf{A}_t^0, \dots, \mathbf{A}_t^1 | \mathbf{o}_t)}{\pi_{\theta, \text{old}}(\mathbf{A}_t^0, \dots, \mathbf{A}_t^1 | \mathbf{o}_t)} \right)^s, \quad (6)$$

$$\mathcal{L}_{\text{PPOFlow}}(\theta, \phi) = \mathbb{E}_t \left[\min \left(\hat{r}_t \hat{A}_t, \text{clip}(\hat{r}_t, 1 - \epsilon, 1 + \epsilon) \hat{A}_t \right) \right], \quad (7)$$

where \hat{A}_t is the advantage estimate computed with GAE [45], ϵ is the clipping range, and $s \in (0, 1]$ is a scaling factor that reduces variance and helps enforce the importance ratio to stay within a more stable numerical range [46].

4 Experiments

Experiment design. To study the effect of scaling the number of scenes N , we generate 100 unique scenes and denote this full set as \mathcal{W} (see Sec. C for details and metrics). In this work, we focus on a pick-and-place task in which, given a language command, the policy must grasp an object and place it on top of another amid several distractors. For embodiment, we use the same Interbotix WidowX 250S manipulator (Fig. 4) as in Bridge.

A single external Logitech C922 webcam is used for vision. Real-world evaluation is conducted on an NVIDIA RTX 4090 GPU. To evaluate out-of-distribution (OOD) generalization, we construct three randomly sampled subsets of \mathcal{W} , each containing 50 scenes, denoted \mathcal{H}_i for $i \in \{0, 1, 2\}$. For each subset, the corresponding OOD set is defined as $\bar{\mathcal{H}}_i = \mathcal{W} \setminus \mathcal{H}_i$. Using each \mathcal{H}_i , we train three independent runs for each $N \in \{1, 3, 10, 25, 50\}$, where training uses the first N scenes under a fixed ordering of \mathcal{H}_i . In addition, we train a single run on the full set \mathcal{W} . The initial flow-matching imitation policy π_{pre} serves as a baseline and uses $K = 10$ and action chunk size $C = 4$. To investigate the benefits of training on generated scenes, we introduce another baseline where we RL fine-tune a policy on three manually designed Bridge tabletop scenes from *SimplerEnv* [47].

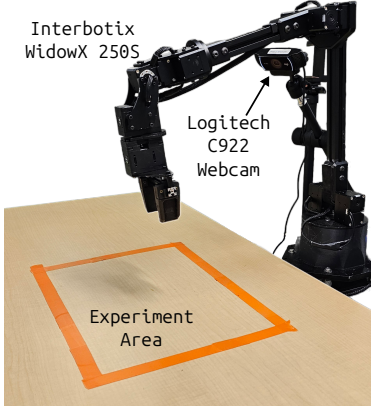


Figure 4: Experiment overview.

Training details. For training, we use 8 NVIDIA RTX 6000 Ada GPUs to LoRA fine-tune the VLM E_θ and fully fine-tune the action expert v_θ over 5 days. The value head V_ψ and noise head σ_ϕ are shallow MLPs and are also fully fine-tuned. Training curves are shown in Fig. 5. To enable successful sim-to-real transfer, we rely on three factors: (1) the digital twin-like fidelity of generated objects and scenes, (2) domain randomization, and (3) PD control with gravity compensation. With gravity compensation enabled, we found that explicit system identification was largely unnecessary, provided that both simulation and real-world controllers could reach the majority of target poses with sufficiently low tracking error, thereby minimizing the dynamics sim-to-real gap. We use an action chunk size of $C = 4$ and set the number of integration steps to $K = 1$. All other training hyperparameters and domain randomization ranges are provided in Tables A.1 and A.2, respectively. Note that in Fig. 5, the final training success rates decrease monotonically as N increases. This behavior is expected, as we use the same batch size and mini-batch size for all runs; consequently, each scene receives fewer samples, scaling linearly with $1/N$. We hypothesize that scaling the batch size and mini-batch size proportionally with N could mitigate this effect. However, as shown in the next section, higher training success rates with low N do not necessarily translate to improved OOD performance.

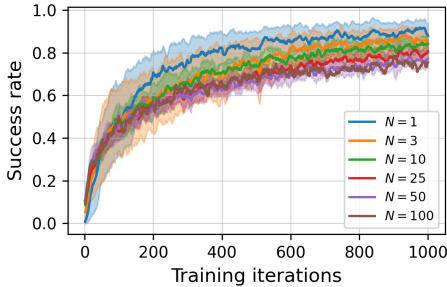


Figure 5: Training curves for all N .

Effect of number of scenes N . Table 1 reports simulation results as a function of the number of training scenes N . We evaluate both average success rate (SR) and average time to finish (TF) across four different sets of evaluation scenes. Results reported with standard deviation are averaged over three independent runs trained on different subsets \mathcal{H}_i . Each scene is evaluated over 100 episodes.

For policies trained on EmbodiedGen (EG) scenes, increasing N produces a clear trade-off between in-distribution (ID) and out-of-distribution (OOD) performance. As N increases, the success rate on the training scenes \mathcal{H}_i decreases, which is expected given the fixed mini-batch size used during training, while success rates on both EG OOD scenes $\bar{\mathcal{H}}_i$ and the *SimplerEnv* (SE) scenes increase steadily. For example, ID success decreases from 94.3% at $N = 1$ to 78.9% at $N = 50$, while EG OOD success improves from 53.2% to 77.9%. Similarly, SE success increases from 36.1% to 68.4%.

Increasing N also substantially reduces the gap between ID and OOD performance. At $N = 1$, the gap between EG ID and EG OOD success rates is 41.1 percentage points (94.3% vs. 53.2%). This gap shrinks to 27.4 points at $N = 3$, 9.3 points at $N = 10$, and only 1.0 point at $N = 50$. A similar trend is observed for SE evaluation, where the gap between EG ID and SE success decreases from 58.2 points at $N = 1$ to 10.5 points at $N = 50$. These results indicate that increasing scene diversity reduces over-specialization to training environments and improves cross-scene generalization. These

Table 1: Simulation evaluation results. EG: EmbodiedGen. SE: SimplerEnv. For a certain policy (row), the evaluation results are colored coded as OOD, ID, and mixture.

Policy	EG ID scenes $\mathcal{H}_i (N)$		EG OOD scenes $\bar{\mathcal{H}}_i (50)$		EG all scenes $\mathcal{W} (100)$		SE scenes (3)	
	SR (%) [\uparrow]	TF (s) [\downarrow]	SR (%) [\uparrow]	TF (s) [\downarrow]	SR (%) [\uparrow]	TF (s) [\downarrow]	SR (%) [\uparrow]	TF (s) [\downarrow]
$N = 0$ (π_{pre})	—	—	9.6	10.3	9.7	10.0	23.7	9.6
$N = 3$ (SE)	—	—	36.5	8.5	36.0	8.6	96.7	6.7
$N = 1$	94.3 \pm 2.6	7.7 \pm 0.9	53.2 \pm 5.5	9.0 \pm 0.5	51.6 \pm 5.3	9.0 \pm 0.3	36.1 \pm 10.4	9.3 \pm 1.7
$N = 3$	88.7 \pm 4.7	7.6 \pm 0.5	61.3 \pm 1.8	8.7 \pm 0.5	60.0 \pm 4.6	8.8 \pm 0.5	47.4 \pm 2.3	9.8 \pm 0.6
$N = 10$	81.7 \pm 9.5	8.3 \pm 0.8	72.4 \pm 0.4	8.2 \pm 0.2	72.1 \pm 0.9	8.2 \pm 0.1	54.3 \pm 9.2	9.2 \pm 0.4
$N = 25$	85.2 \pm 4.1	8.0 \pm 0.4	77.6 \pm 0.8	8.1 \pm 0.2	78.3 \pm 0.5	8.1 \pm 0.1	70.1 \pm 5.4	8.4 \pm 0.1
$N = 50$	78.9 \pm 12.1	8.1 \pm 0.8	77.9 \pm 0.9	8.0 \pm 0.2	79.2 \pm 0.3	7.9 \pm 0.1	68.4 \pm 5.5	8.5 \pm 0.6
$N = 100$	—	—	—	—	79.8	8.0	74.3	8.4

trends suggest that scene diversity encourages the policy to learn task-level manipulation strategies rather than scene-specific behaviors. Notably, the $N = 100$ policy achieves the best performance on SE scenes (74.3%) despite never being trained on those environments.

In contrast, the policy trained on the three manually designed SE scenes achieves very high success on those same scenes (96.7%) but exhibits the largest performance drop when evaluated on EG environments (36.5% OOD SR), a 60.2-point gap. This highlights the limited coverage of the SE scenes compared to the greater diversity provided by EG-generated environments. Finally, training on the full scene set yields the strongest overall performance. Compared to the imitation baseline π_{pre} ($N = 0$), the $N = 100$ policy improves success rate on EG scenes from 9.7% to 79.8%, while reducing average completion time from about 10 s to 8 s.

Sim-to-real performance. Table 2 reports sim-to-real evaluation results across 12 scenes and 240 real-world trials. Each experiment consists of 10 trials for both the imitation baseline π_{pre} and the $N = 100$ RL fine-tuned policy. We report partial success rate (PSR), defined as correctly grasping and lifting the target object, overall task success rate (SR), dynamics failure rate (DFR), semantics failure rate (SFR), and time to finish (TF). DFR measures failures caused by execution errors such as inaccurate grasp attempts or dropped objects, while SFR measures failures caused by incorrect task interpretation (e.g., interacting with the wrong object). These failure categories are not mutually exclusive, as a single failure may involve both semantic and dynamics-related errors.

Overall performance improves substantially after RL fine-tuning. Partial success increases from 45% for π_{pre} to 88.3%, indicating a large improvement in reliable object acquisition. Overall task success improves even more, increasing from 21.7% to 75%. In addition to higher success rates, the RL policy produces more efficient behavior, reducing the average completion time from 11.5 s to 10.2 s.

Examining the failure breakdown reveals that most errors of the imitation baseline arise from dynamics-related issues. Across all trials, the baseline exhibits a DFR of 66.7%, which decreases to 18.3% after RL fine-tuning, indicating a substantial improvement in manipulation robustness. Semantic failures are comparatively less frequent but also decrease from 18.3% to 6.7%, suggesting improved task grounding and object selection.

Performance gains are consistent across nearly all scenes. For example, scene 10 introduces a screwdriver that does not appear in the RL training distribution, yet the RL policy achieves an SR of 50% compared to 0% for the baseline. Similarly, scene 11 evaluates a teacup stacking task involving unseen object instances and task composition, where the RL policy improves SR from 20% to 50% while maintaining perfect partial success (100%).

Overall, these results demonstrate that policies fine-tuned in large-scale generative simulation transfer effectively to real-world manipulation. RL fine-tuning improves both low-level execution robustness and high-level task success while maintaining generalization to previously unseen objects, attributes, and task variations. Qualitative examples of the imitation and RL policy rollouts across different scenes are shown in Sec. H.

Table 2: Sim-to-real evaluation results. Objects or attributes that are OOD during RL training are **highlighted**. Attributes in parentheses were not included in the language command. Columns are color coded as `success`, `failure`, and `time` metrics.

Scene	Language Command	Scene Distractors
0	“put the banana on the bowl.”	broccoli, strawberry, plate
1	“put the broccoli on the mug.”	knife, cutting board
2	“put the mushroom on the bowl.”	banana, broccoli, plate
3	“put the spoon on the napkin.”	fork, plate
4	“put the (pink) eraser on the notebook.”	black pen, mug
5	“put the (yellow) brush on the bowl.”	banana, yellow marker
6	“put the white eraser on the mug.”	pink eraser, black pen, blue pen
7	“put the red knife on the cutting board.”	regular knife
8	“put the blue pen on the (blue) bowl.”	black pen, white eraser, basket
9	“put the green marker on the basket.”	red marker, yellow marker, dry erase eraser, cardboard box
10	“put the screwdriver on the basket.”	knife, black marker
11	“put the blue teacup on the yellow teacup.”	purple teacup, pink teapot, blue plate, yellow plate

	Imitation baseline π_{pre}					$N = 100$				
	PSR [\uparrow]	SR [\uparrow]	DFR [\downarrow]	SFR [\downarrow]	TF (s) [\downarrow]	PSR [\uparrow]	SR [\uparrow]	DFR [\downarrow]	SFR [\downarrow]	TF (s) [\downarrow]
0	0.8	0.6	0.4	0.0	10.7 \pm 6.3	0.9	0.9	0.1	0.0	7.4 \pm 1.5
1	0.4	0.2	0.8	0.0	13.3 \pm 2.0	1.0	0.7	0.3	0.0	10.4 \pm 7.5
2	0.3	0.1	0.9	0.0	11.5	0.9	0.9	0.1	0.0	8.4 \pm 2.5
3	0.2	0.1	0.7	0.5	6.1	0.8	0.7	0.1	0.2	12.2 \pm 5.1
4	0.4	0.3	0.7	0.1	11.0 \pm 4.9	1.0	1.0	—	—	10.2 \pm 4.2
5	0.6	0.3	0.7	0.0	10.5 \pm 1.1	1.0	1.0	—	—	9.5 \pm 3.9
6	0.4	0.2	0.8	0.0	7.8 \pm 0.1	1.0	0.7	0.3	0.0	11.1 \pm 5.5
7	0.7	0.2	0.2	0.6	14.6 \pm 0.6	0.8	0.8	0.0	0.2	12.2 \pm 6.5
8	0.3	0.1	0.9	0.0	29.6	0.9	0.7	0.2	0.1	12.2 \pm 7.4
9	0.6	0.3	0.6	0.1	9.2 \pm 1.8	0.7	0.6	0.4	0.0	8.8 \pm 2.0
10	0.2	0.0	0.8	0.3	—	0.6	0.5	0.2	0.3	10.4 \pm 5.5
11	0.5	0.2	0.5	0.6	11.6 \pm 2.0	1.0	0.5	0.5	0.0	11.0 \pm 2.0
All	0.45	0.217	0.667	0.183	11.5 \pm 5.5	0.883	0.75	0.183	0.067	10.2 \pm 5.1

5 Conclusion

In this work, we explored the use of 3D world generative models for scaling sim-to-real reinforcement learning of vision–language–action (VLA) policies. By leveraging generative simulation to automatically construct diverse interactive environments, we fine-tuned a pretrained VLA across 100 unique scenes using massively parallel RL while avoiding the cost of manual scene design. Our results show that increasing scene diversity significantly improves zero-shot generalization across multiple OOD evaluation scenes. Furthermore, RL fine-tuning on the generated scenes improves simulation success rates by 70.1 percentage points, while sim-to-real deployment yields a 53.3-percentage-point improvement in real-world task success. Beyond improved performance, our findings highlight the complementary roles of generative simulation and RL. Generative 3D world models provide a scalable source of diverse training environments, while RL enables efficient adaptation of large pretrained policies using only sparse rewards. Our language-driven scene designer further reduces engineering effort by automatically translating task descriptions into structured environments for simulation. Together, these components form a practical pipeline for scaling robot foundation models while minimizing the need for additional real-world data collection or human-in-the-loop training.

Limitations and future work. We note that the experiments in this work focus on pick-and-place tasks, primarily due to current limitations in the types of objects and interactions that EmbodiedGen [42] can reliably generate. Looking forward, we aim to extend EmbodiedGen to support richer manipulation behaviors such as articulated object manipulation, tool use, and multi-stage tasks. Scaling the distribution of automatically generated scenes and tasks will enable RL fine-tuning of VLAs on a broader range of interaction distributions, further improving generalization and robustness. Nevertheless, we believe this work represents an important first step toward demonstrating the potential of combining generative simulation with RL to scale the fine-tuning of VLA models.

References

- [1] O. X.-E. Collaboration. Open X-Embodiment: Robotic learning datasets and RT-X models. <https://arxiv.org/abs/2310.08864>, 2023.
- [2] S. Deng, M. Yan, S. Wei, H. Ma, Y. Yang, J. Chen, Z. Zhang, T. Yang, X. Zhang, W. Zhang, H. Cui, Z. Zhang, and H. Wang. Graspvla: a grasping foundation model pre-trained on billion-scale synthetic action data, 2025. URL <https://arxiv.org/abs/2505.03233>.
- [3] Y. Chen, S. Tian, S. Liu, Y. Zhou, H. Li, and D. Zhao. Conrft: A reinforced fine-tuning method for vla models via consistency policy. In *Proceedings of Robotics: Science and Systems, RSS 2025, Los Angeles, CA, USA, Jun 21-25, 2025*, 2025. doi:10.15607/RSS.2025.XXI.019.
- [4] P. Intelligence, A. Amin, R. Aniceto, A. Balakrishna, K. Black, K. Conley, G. Connors, J. Darpinian, K. Dhabalia, J. DiCarlo, D. Driess, M. Equi, A. Esmail, Y. Fang, C. Finn, C. Glossop, T. Godden, I. Goryachev, L. Groom, H. Hancock, K. Hausman, G. Hussein, B. Ichter, S. Jakubczak, R. Jen, T. Jones, B. Katz, L. Ke, C. Kuchi, M. Lamb, D. LeBlanc, S. Levine, A. Li-Bell, Y. Lu, V. Mano, M. Mothukuri, S. Nair, K. Pertsch, A. Z. Ren, C. Sharma, L. X. Shi, L. Smith, J. T. Springenberg, K. Stachowicz, W. Stoeckle, A. Swerdlow, J. Tanner, M. Torne, Q. Vuong, A. Walling, H. Wang, B. Williams, S. Yoo, L. Yu, U. Zhilinsky, and Z. Zhou. $\pi_{0,6}^*$: a vla that learns from experience, 2025. URL <https://arxiv.org/abs/2511.14759>.
- [5] H. Li, Y. Zuo, J. Yu, Y. Zhang, Z. Yang, K. Zhang, X. Zhu, Y. Zhang, T. Chen, G. Cui, D. Wang, D. Luo, Y. Fan, Y. Sun, J. Zeng, J. Pang, S. Zhang, Y. Wang, Y. Mu, B. Zhou, and N. Ding. Simplevla-rl: Scaling vla training via reinforcement learning, 2025. URL <https://arxiv.org/abs/2509.09674>.
- [6] J. Schulman, F. Wolski, P. Dhariwal, A. Radford, and O. Klimov. Proximal policy optimization algorithms, 2017. URL <https://arxiv.org/abs/1707.06347>.
- [7] T. Zhang, C. Yu, S. Su, and Y. Wang. Reinfo: Fine-tuning flow matching policy with online reinforcement learning. In *The Thirty-ninth Annual Conference on Neural Information Processing Systems*, 2025. URL <https://openreview.net/forum?id=ACagRwCCqu>.
- [8] A. Z. Ren, J. Lidard, L. L. Ankile, A. Simeonov, P. Agrawal, A. Majumdar, B. Burchfiel, H. Dai, and M. Simchowitz. Diffusion policy policy optimization. In *arXiv preprint arXiv:2409.00588*, 2024.
- [9] C. Pan, G. Anantharaman, N.-C. Huang, C. Jin, D. Pfrommer, C. Yuan, F. Permenter, G. Qu, N. Boffi, G. Shi, and M. Simchowitz. Much ado about noising: Dispelling the myths of generative robotic control, 2025. URL <https://arxiv.org/abs/2512.01809>.
- [10] Y. Chen, H. Li, and D. Zhao. Boosting continuous control with consistency policy, 2024. URL <https://arxiv.org/abs/2310.06343>.
- [11] A. Prasad, K. Lin, J. Wu, L. Zhou, and J. Bohg. Consistency policy: Accelerated visuomotor policies via consistency distillation, 2024. URL <https://arxiv.org/abs/2405.07503>.
- [12] H. Walke, K. Black, A. Lee, M. J. Kim, M. Du, C. Zheng, T. Zhao, P. Hansen-Estruch, Q. Vuong, A. He, V. Myers, K. Fang, C. Finn, and S. Levine. Bridgedata v2: A dataset for robot learning at scale. In *Conference on Robot Learning (CoRL)*, 2023.
- [13] T. Chen, Z. Chen, B. Chen, Z. Cai, Y. Liu, Q. Liang, Z. Li, X. Lin, Y. Ge, Z. Gu, et al. Robotwin 2.0: A scalable data generator and benchmark with strong domain randomization for robust bimanual robotic manipulation. *arXiv preprint arXiv:2506.18088*, 2025.
- [14] M. J. Kim, K. Pertsch, S. Karamcheti, T. Xiao, A. Balakrishna, S. Nair, R. Rafailov, E. Foster, G. Lam, P. Sanketi, Q. Vuong, T. Kollar, B. Burchfiel, R. Tedrake, D. Sadigh, S. Levine, P. Liang, and C. Finn. Openvla: An open-source vision-language-action model, 2024. URL <https://arxiv.org/abs/2406.09246>.

- [15] D. Qu, H. Song, Q. Chen, Y. Yao, X. Ye, Y. Ding, Z. Wang, J. Gu, B. Zhao, D. Wang, and X. Li. Spatialvla: Exploring spatial representations for visual-language-action model, 2025. URL <https://arxiv.org/abs/2501.15830>.
- [16] K. Black, N. Brown, D. Driess, A. Esmail, M. Equi, C. Finn, N. Fusai, L. Groom, K. Hausman, B. Ichter, S. Jakubczak, T. Jones, L. Ke, S. Levine, A. Li-Bell, M. Mothukuri, S. Nair, K. Pertsch, L. X. Shi, J. Tanner, Q. Vuong, A. Walling, H. Wang, and U. Zhilinsky. π_0 : A vision-language-action flow model for general robot control, 2024. URL <https://arxiv.org/abs/2410.24164>.
- [17] P. Intelligence, K. Black, N. Brown, J. Darpinian, K. Dhabalia, D. Driess, A. Esmail, M. Equi, C. Finn, N. Fusai, M. Y. Galliker, D. Ghosh, L. Groom, K. Hausman, B. Ichter, S. Jakubczak, T. Jones, L. Ke, D. LeBlanc, S. Levine, A. Li-Bell, M. Mothukuri, S. Nair, K. Pertsch, A. Z. Ren, L. X. Shi, L. Smith, J. T. Springenberg, K. Stachowicz, J. Tanner, Q. Vuong, H. Walke, A. Walling, H. Wang, L. Yu, and U. Zhilinsky. $\pi_{0.5}$: a vision-language-action model with open-world generalization, 2025. URL <https://arxiv.org/abs/2504.16054>.
- [18] M. J. Kim, C. Finn, and P. Liang. Fine-tuning vision-language-action models: Optimizing speed and success, 2025. URL <https://arxiv.org/abs/2502.19645>.
- [19] J. Liu, F. Gao, B. Wei, X. Chen, Q. Liao, Y. Wu, C. Yu, and Y. Wang. What can rl bring to vla generalization? an empirical study, 2026. URL <https://arxiv.org/abs/2505.19789>.
- [20] Y. Xing, X. Luo, J. Xie, L. Gao, H. Shen, and J. Song. Shortcut learning in generalist robot policies: The role of dataset diversity and fragmentation, 2025. URL <https://arxiv.org/abs/2508.06426>.
- [21] A. Sharma, A. M. Ahmed, R. Ahmad, and C. Finn. Self-improving robots: End-to-end autonomous visuomotor reinforcement learning. In *7th Annual Conference on Robot Learning*, 2023. URL <https://openreview.net/forum?id=ApXLUk8U-1>.
- [22] S. K. S. Ghasemipour, A. Wahid, J. Tompson, P. R. Sanketi, and I. Mordatch. Self-improving embodied foundation models. In *The Thirty-ninth Annual Conference on Neural Information Processing Systems*, 2025. URL <https://openreview.net/forum?id=KXMIIUVB9U>.
- [23] J. Yang, M. S. Mark, B. Vu, A. Sharma, J. Bohg, and C. Finn. Robot fine-tuning made easy: Pre-training rewards and policies for autonomous real-world reinforcement learning. In *2024 IEEE International Conference on Robotics and Automation (ICRA)*, pages 4804–4811, 2024. doi:10.1109/ICRA57147.2024.10610421.
- [24] H. R. Walke, J. H. Yang, A. Yu, A. Kumar, J. Orbik, A. Singh, and S. Levine. Don’t start from scratch: Leveraging prior data to automate robotic reinforcement learning. In K. Liu, D. Kulic, and J. Ichnowski, editors, *Proceedings of The 6th Conference on Robot Learning*, volume 205 of *Proceedings of Machine Learning Research*, pages 1652–1662. PMLR, 14–18 Dec 2023. URL <https://proceedings.mlr.press/v205/walke23a.html>.
- [25] R. Mendonca and D. Pathak. Continuously improving mobile manipulation with autonomous real-world RL. In *RSS 2024 Workshop: Data Generation for Robotics*, 2024. URL <https://openreview.net/forum?id=qASoq07bXh>.
- [26] Y. Du, K. Konyushkova, M. Denil, A. Raju, J. Landon, F. Hill, N. de Freitas, and S. Cabi. Vision-language models as success detectors, 2023. URL <https://arxiv.org/abs/2303.07280>.
- [27] Y. Fang, Y. Yang, X. Zhu, K. Zheng, G. Bertasius, D. Szafir, and M. Ding. Rebot: Scaling robot learning with real-to-sim-to-real robotic video synthesis, 2025. URL <https://arxiv.org/abs/2503.14526>.

- [28] H. Li, P. Ding, R. Suo, Y. Wang, Z. Ge, D. Zang, K. Yu, M. Sun, H. Zhang, D. Wang, and W. Su. Vla-rft: Vision-language-action reinforcement fine-tuning with verified rewards in world simulators, 2025. URL <https://arxiv.org/abs/2510.00406>.
- [29] H. Zhang, H. Yu, L. Zhao, A. Choi, Q. Bai, Y. Yang, and W. Xu. Learning multi-stage pick-and-place with a legged mobile manipulator. *IEEE Robotics and Automation Letters*, 10(11): 11419–11426, 2025. doi:10.1109/LRA.2025.3608425.
- [30] R. Singh, A. Allshire, A. Handa, N. Ratliff, and K. V. Wyk. Dextrah-rgb: Visuomotor policies to grasp anything with dexterous hands, 2025. URL <https://arxiv.org/abs/2412.01791>.
- [31] P. Dan, K. Kedia, A. Chao, E. Duan, M. A. Pace, W.-C. Ma, and S. Choudhury. X-sim: Cross-embodiment learning via real-to-sim-to-real. In *9th Annual Conference on Robot Learning*, 2025. URL <https://openreview.net/forum?id=B07qo66YJ2>.
- [32] Z. Chen, Q. Yan, Y. Chen, T. Wu, J. Zhang, Z. Ding, J. Li, Y. Yang, and H. Dong. Clutter-dexgrasp: A sim-to-real system for general dexterous grasping in cluttered scenes. In *9th Annual Conference on Robot Learning*, 2025. URL <https://openreview.net/forum?id=4XKKUifQ9c>.
- [33] T. He, Z. Wang, H. Xue, Q. Ben, Z. Luo, W. Xiao, Y. Yuan, X. Da, F. Castañeda, S. Sastry, C. Liu, G. Shi, L. Fan, and Y. Zhu. Viral: Visual sim-to-real at scale for humanoid loco-manipulation, 2025. URL <https://arxiv.org/abs/2511.15200>.
- [34] T. He, J. Gao, W. Xiao, Y. Zhang, Z. Wang, J. Wang, Z. Luo, G. He, N. Sobanbab, C. Pan, Z. Yi, G. Qu, K. Kitani, J. Hodgins, L. J. Fan, Y. Zhu, C. Liu, and G. Shi. Asap: Aligning simulation and real-world physics for learning agile humanoid whole-body skills, 2025. URL <https://arxiv.org/abs/2502.01143>.
- [35] M. Wang, S. Tian, A. Swann, O. Shorinwa, J. Wu, and M. Schwager. Phys2real: Fusing vlm priors with interactive online adaptation for uncertainty-aware sim-to-real manipulation, 2025. URL <https://arxiv.org/abs/2510.11689>.
- [36] H. Sun, H. Wang, C. Ma, S. Zhang, J. Ye, X. Chen, and X. Lan. Prism: Projection-based reward integration for scene-aware real-to-sim-to-real transfer with few demonstrations, 2025. URL <https://arxiv.org/abs/2504.20520>.
- [37] T. G. W. Lum, O. Y. Lee, K. Liu, and J. Bohg. Crossing the human-robot embodiment gap with sim-to-real RL using one human demonstration. In *9th Annual Conference on Robot Learning*, 2025. URL <https://openreview.net/forum?id=CgGSFtjplI>.
- [38] J. Xiang, Z. Lv, S. Xu, Y. Deng, R. Wang, B. Zhang, D. Chen, X. Tong, and J. Yang. Structured 3d latents for scalable and versatile 3d generation, 2025. URL <https://arxiv.org/abs/2412.01506>.
- [39] Z. Xie. Worldgen: Generate any 3d scene in seconds. <https://github.com/ZiYang-xie/WorldGen>, 2025.
- [40] Y. Yang, F.-Y. Sun, L. Weihs, E. VanderBilt, A. Herrasti, W. Han, J. Wu, N. Haber, R. Krishna, L. Liu, C. Callison-Burch, M. Yatskar, A. Kembhavi, and C. Clark. Holodeck: Language guided generation of 3d embodied ai environments, 2024. URL <https://arxiv.org/abs/2312.09067>.
- [41] Y. Wang, Z. Xian, F. Chen, T.-H. Wang, Y. Wang, K. Fragkiadaki, Z. Erickson, D. Held, and C. Gan. Robogen: Towards unleashing infinite data for automated robot learning via generative simulation, 2024. URL <https://arxiv.org/abs/2311.01455>.
- [42] X. Wang, L. Liu, Y. Cao, R. Wu, W. Qin, D. Wang, W. Sui, and Z. Su. Embodiedgen: Towards a generative 3d world engine for embodied intelligence, 2025. URL <https://arxiv.org/abs/2506.10600>.

- [43] S. Tao, F. Xiang, A. Shukla, Y. Qin, X. Hinrichsen, X. Yuan, C. Bao, X. Lin, Y. Liu, T. kai Chan, Y. Gao, X. Li, T. Mu, N. Xiao, A. Gurha, V. N. Rajesh, Y. W. Choi, Y.-R. Chen, Z. Huang, R. Calandra, R. Chen, S. Luo, and H. Su. Maniskill3: Gpu parallelized robotics simulation and rendering for generalizable embodied ai. *Robotics: Science and Systems*, 2025.
- [44] J. Achiam, S. Adler, S. Agarwal, L. Ahmad, I. Akkaya, F. L. Aleman, D. Almeida, J. Altenschmidt, S. Altman, S. Anadkat, et al. Gpt-4 technical report. *arXiv preprint arXiv:2303.08774*, 2023.
- [45] J. Schulman, P. Moritz, S. Levine, M. Jordan, and P. Abbeel. High-dimensional continuous control using generalized advantage estimation, 2018. URL <https://arxiv.org/abs/1506.02438>.
- [46] C. Zheng, S. Liu, M. Li, X.-H. Chen, B. Yu, C. Gao, K. Dang, Y. Liu, R. Men, A. Yang, J. Zhou, and J. Lin. Group sequence policy optimization, 2025. URL <https://arxiv.org/abs/2507.18071>.
- [47] X. Li, K. Hsu, J. Gu, K. Pertsch, O. Mees, H. R. Walke, C. Fu, I. Lunawat, I. Sieh, S. Kirmani, S. Levine, J. Wu, C. Finn, H. Su, Q. Vuong, and T. Xiao. Evaluating real-world robot manipulation policies in simulation, 2024. URL <https://arxiv.org/abs/2405.05941>.
- [48] A. Wagenmaker, M. Nakamoto, Y. Zhang, S. Park, W. Yagoub, A. Nagabandi, A. Gupta, and S. Levine. Steering your diffusion policy with latent space reinforcement learning, 2025. URL <https://arxiv.org/abs/2506.15799>.
- [49] D. McAllister, S. Ge, B. Yi, C. M. Kim, E. Weber, H. Choi, H. Feng, and A. Kanazawa. Flow matching policy gradients, 2025. URL <https://arxiv.org/abs/2507.21053>.

A Training Details

In this section, we list the training parameters used for all policies in Table A.1. We also summarize several practical observations encountered during training:

1. Several training strategies were evaluated, including:
 - (a) Freezing the VLM and LoRA fine-tuning the action head.
 - (b) Freezing the VLM and fully fine-tuning the action head.
 - (c) Freezing the SigLip vision encoder, LoRA fine-tuning Gemma, and LoRA fine-tuning the action head.
 - (d) LoRA fine-tuning the VLM and LoRA fine-tuning the action head.
 - (e) LoRA fine-tuning the VLM and fully fine-tuning the action head.

Overall, we found that freezing the VLM (a, b) significantly lowers the training ceiling and often leads to model collapse during prolonged training, where task success rates initially peak, then saturate, and eventually decline toward zero. As a result, updating the VLM is crucial for stable learning. Fully fine-tuning the action head consistently outperformed the corresponding configuration that LoRA fine-tunes it. Freezing the SigLip vision encoder reduced success rates monotonically by a few percent compared to LoRA fine-tuning it. Since LoRA fine-tuning the entire VLM did not noticeably affect sim-to-real performance, we adopt option (e) in this work.

2. Adding the scaling exponent s to the importance ratio (Eq. 6) is crucial for stabilizing training and preventing immediate collapse. Without it, the computed log probabilities can spike to very large values, causing many updates to fall near the clipping threshold and resulting in the majority of gradients being clipped.

Table A.1: Training parameters.

Parameter	Value	Parameter	Value
number of environments	192	action chunk size C	4
batch size	19200	number of integration steps K	1
mini batch size	1920	learning rate	$2e-5$
episode length	25	gradient global norm clip	0.5
discount factor γ	0.99	clipping ratio ϵ	0.2
UTD ratio	1	importance ratio scale s	0.2
LoRA rank	32	σ_ϕ log min	-2.5
control frequency (Hz)	5	σ_ϕ log max	-2.0

Domain randomization. Domain randomization ranges can be seen in Table A.2. For lighting, we use the same lighting setup as the one in SimplerEnv’s Bridge setting [47]. For camera position randomization, we first record the intersection point between the camera’s principal ray and the table in the default configuration. We then compute a new camera orientation such that the principal ray of the perturbed camera re-aligns with this original intersection point. We found that control-delay randomization was unnecessary due to the use of action chunks ($C = 4$), which allow the majority of actions to be executed with minimal latency.

Table A.2: Domain randomization ranges.

Parameter	Value	Parameter	Value
object x-position (m)	$[0.2, 0.4]$	robot z-height perturb (m)	$[0, 0.05]$
object y-position (m)	$[-0.15, 0.15]$	robot joint pos perturb (rad)	$[-0.1, 0.1]^6$
object yaw orientation (rad)	$[0, 2\pi]$	camera xyz-position (m)	$[-0.05, 0.05]^3$
ambient light RGB color	$[0, 0.6]^3$	directional light brightness	$[0.5, 1.5]$

Rewards. We employ a sparse success reward, enabled by the strong pre-training of the VLA during the imitation phase. An episode is considered successful if

$$\text{success} = \text{contact}(A, B) \wedge \neg \text{contact}(A, \text{table}) \wedge \neg \text{contact}(A, \text{robot}), \quad (8)$$

where A denotes the manipulated object and B denotes the target object onto which A is placed.

B Does Multimodality Matter? Effect of K

In this work, we set $K = 1$, effectively converting the flow-matching policy π_{pre} into a single-step Gaussian policy π_{θ} during RL fine-tuning. While prior work such as Diffusion Steering [48] and Flow Policy Optimization (FPO) [49] demonstrate that flow-matching models can be fine-tuned without collapsing into a Gaussian policy, we found that: (1) PPOFlow led to significantly more stable and repeatable training, and (2) single-step ($K = 1$) RL fine-tuning exhibited no observable degradation in policy performance compared to maintaining multimodality ($K > 1$).

We validate the latter through an ablation over $K \in \{1, 2, 4\}$ on the entire scene–task set \mathcal{W} , where larger K enables greater expressivity by chaining multiple Gaussian transitions, with $K = 1$ corresponding to a unimodal policy. From the left side of Table B.1, increasing K does not improve performance; in fact, $K = 1$ achieves the highest success rate. Although the margin is modest (approximately 2–2.5%) and based on a single run, these results suggest that multimodality does not meaningfully benefit RL fine-tuning in this setting. Our findings align with recent work by Pan et al. [9], which argues that multimodality is not the primary driver of diffusion-based policy performance in robot manipulation. We hypothesize that multimodality is most beneficial during imitation learning when the demonstration distribution itself is multimodal [8]. In contrast, under reward-guided optimization, unimodal Gaussian policies appear sufficient for effective policy improvement.

Beyond maintaining competitive performance, reducing K substantially improves computational efficiency. As shown in Table B.1, $K = 1$ achieves a $1.17\times$ speedup in backward pass time relative to $K = 2$ and a $1.45\times$ speedup relative to $K = 4$. Inference gains are even more pronounced. Compared to the original imitation setting of $K = 10$, $K = 1$ yields a $2.72\times$ speedup in inference latency under a regular forward pass and a $2.36\times$ speedup when using `torch.compile`. These improvements stem from eliminating iterative denoising steps, effectively reducing the policy to a single forward pass, similar in spirit to consistency policies [10, 11, 3]. Overall, these results suggest that multimodality offers limited benefit during RL fine-tuning while incurring significant computational overhead.

Table B.1: Effect of K on RL fine-tuning and inference.

K	RL SR (%) [↑]	RL TF (s) [↓]	Backward Time (s) [↓]	Inference Latency (s) [↓]	
				Reg.	<code>torch.compile</code>
$K = 10$	N/A	N/A	N/A	0.267	0.172
$K = 4$	77.29	7.76	108.80	0.153	0.107
$K = 2$	77.23	8.36	87.55	0.120	0.086
$K = 1$	79.75	7.94	74.74	0.098	0.073

C Generative Simulation Metrics

Table C.1 reports the profiling statistics of the generative simulation pipeline illustrated in Fig. 2. Across 100 generated environments, the system produces 516 unique object assets, averaging 5.16 interactive objects per scene. Because the asset generation pipeline proceeds from text to a background-removed foreground image and then to a 3D asset, we deploy a GPT-4o-based automated quality assurance (QA) loop at multiple stages. The *Semantic Appearance checker* serves as an early filter on the intermediate foreground image, verifying whether it matches the target object category and key visual attributes. If this check fails, the system immediately resamples the text-to-image seed and retries, preventing semantically incorrect intermediate outputs from propagating into the downstream image-to-3D stage. The *Mesh Geometry checker* then evaluates whether the generated 3D mesh is complete and free of major geometric defects. Finally, the *Cross-modal Text-to-3D Alignment checker* assesses whether the final 3D asset remains semantically consistent with the original text description, thereby capturing semantic drift introduced during 3D generation. Combined with this GPT-4o-based QA-driven rejection-and-retry mechanism, assets require only 1.37 generation attempts on average to satisfy all constraints. Manual inspection shows that 85% of the generated environments are directly usable for end-to-end reinforcement learning without human intervention. The remaining failures are mainly due to scale mismatches or imperfect initial object placements (representative failure case see Fig. C.1), which are generally minor and can be rectified with minimal manual adjustment. Under fully online sequential generation on a single NVIDIA RTX 4090 GPU, the pipeline requires 46.8 ± 5.0 minutes per scene. When reusable interactive assets are drawn from a pre-built asset library, the scene generation time is reduced to approximately 2 minutes per environment.

Table C.1: **Profiling statistics of the generative simulation pipeline (Fig. 2).** Results are aggregated over 100 generated scenes under sequential execution on a single NVIDIA RTX 4090 GPU. QA pass rates denote stage-wise single-attempt pass rates, and average attempts are measured per accepted object asset.

Category	Metric	Value
Generation Scale	Total generated environments	100
	Total unique 3D object assets	516
	Avg. interactive assets per scene	5.16
	Total background assets	100
Generation Efficiency	Total time per scene	46.8 ± 5.0 min
	└ Time per background asset	25.0 ± 3.2 min
	└ Time per object asset	3.9 ± 1.6 min
Automated QA Pass Rates	Semantic Appearance	83.3%
	Mesh Geometry	75.2%
	Cross-modal Text-to-3D Alignment	91.9%
	<i>Average attempts per valid asset</i>	1.37
Manual Inspection	Final environment acceptance rate	85%

Auto-scaling of objects. Since the WidowX 250S manipulator (Fig. 4) used in this work has a narrow gripper width of at most 74 mm, many generated objects are too large to be grasped. To address this, we automatically scale down oversized objects (based on their mesh bounding boxes) to ensure they are graspable. We also reduce mesh resolution to simplify contact computation.



Figure C.1: **Representative failure cases in the generative simulation pipeline.** *Top:* failures detected by the automated QA modules, including semantic appearance mismatch, mesh defects, and text-to-3D semantic drift. *Bottom:* residual failures identified by manual inspection after all automated checks pass, including incorrect initialization, scale mismatch, and unstable object placement.

D Foundation Model Candidates

In addition to π_0 , we also considered using OpenVLA [14], but observed a significant real-to-sim performance gap¹. Beyond this gap, the larger size of OpenVLA (7B parameters) compared to π_0 (3B) made the latter a more practical choice. We also evaluated SpatialVLA [15]. Although it had successful real-to-sim transfer, we found its inference latency to be substantially higher than that of π_0 . Overall, we chose π_0 for its small model size (3B), good real-to-sim transfer, and low inference latency.

We note that, rather than using the π_0 model released by Physical Intelligence, we adopt a model provided by a third-party repository (<https://github.com/allenzren/open-pi-zero>) as it includes a checkpoint pretrained on BridgeV2 data.

¹See <https://github.com/openvla/openvla/issues/7#issuecomment-2330572696> for analysis by the authors on the OpenVLA real-to-sim gap.

E SimplerEnv Scenes



Figure E.2: SimplerEnv scenes with domain randomization used for training and evaluation.

We use the three manually designed tabletop scenes from SimplerEnv [47] to both train a $N = 3$ baseline policy and as OOD evaluation scenes for EmbodiedGen scene trained policies. To be able to use the same domain randomization techniques as those in Table A.2, we remove the static png background so that camera pose and lighting randomization can properly take effect (Fig. E.2).

F Simulation Scenes and Per-scene Results

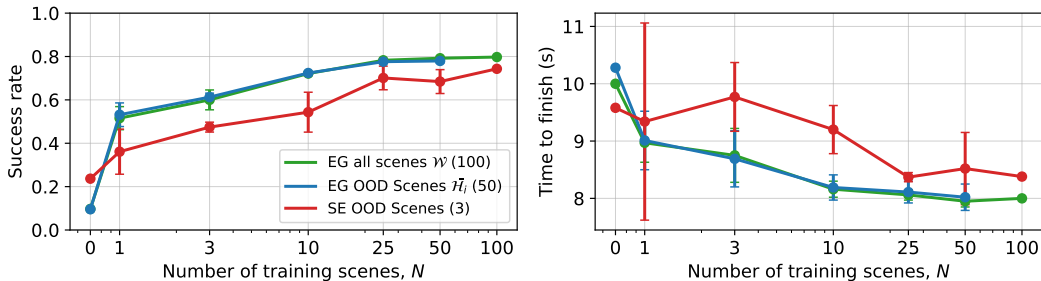


Figure F.3: Success rate and time to finish as a function of N . EG: EmbodiedGen. SE: SimplerEnv.

In this section, we provide a textual description of each scene in \mathcal{W} (see Tables F.1 and F.2). We additionally report the individual success rates for each scene in \mathcal{W} for the policies listed in Table 1, shown in Figs. F.4, F.5, F.6, and F.7. Finally, a plot version of Table 1 (partially) is shown in Fig. F.3 which showcases the monotonic increase in average success rate as N increases.

Table F.1: Generated scenes 0-49.

Scene	Language Command	Scene Distractors
0	green cube → yellow cube	keyboard
1	carrot → plate	knife, bowl
2	ceramic teapot → tray	mug, plate
3	orange → blue napkin	plate
4	banana → red napkin	mug, plate
5	broccoli → white dish	cutting board
6	tomato → saucepan	–
7	cucumber → metal colander	knife, cutting board
8	knife → round container	spoon, plate
9	orange → blue napkin	spoon, plate
10	red cup → tray	fork, plate
11	spoon → black jar	plate
12	pen → round container	book
13	pear → pot	mug, plate
14	apple → plate	book
15	wooden spoon → white plate	glass cup, napkin
16	teacup → plate	spoon, napkin
17	orange → bowl	spoon, plate
18	marker → round container	coffee mug, notebook
19	yellow cup → wooden tray	remote control, book
20	green apple → basket	knife, plate
21	white ping-pong ball → blue cup	remote control, book
22	cucumber → basket	knife, cutting board
23	carrot → plate	knife, cutting board
24	mushroom → pot	knife, cutting board
25	ceramic teapot → tray	mug, plate
26	cucumber → metal colander	knife, cutting board
27	knife → utensil holder	salt shaker, plate
28	orange → napkin	knife, plate
29	lemon → plate	fork, napkin
30	orange → bowl	knife, cutting board
31	tennis ball → gray basket	coffee mug, book
32	marker → round container	coffee mug, notebook
33	yellow cup → wooden tray	fork, napkin
34	green eraser → red box	pen, notebook
35	fork → metal tray	napkin, plate
36	apple → basket	knife, plate
37	spoon → black jar	napkin, plate
38	pen → pen holder	notebook
39	pear → pot	knife, plate
40	teacup → plate	spoon
41	banana → napkin	fork, plate
42	wooden spoon → white plate	salt shaker, napkin
43	marker → pen holder	coffee mug, notebook
44	green apple → basket	salt shaker, plate
45	apple → basket	fork, plate
46	red cup → tray	salt shaker, napkin
47	cucumber → basket	knife, cutting board
48	green apple → fruit bowl	red apple, knife, plate
49	purple cup → tray	spoon, red cup, plate

Table F.2: Generated scenes 50-99.

Scene	Language Command	Distractors
50	white mouse → mouse pad	black mouse, keyboard
51	water bottle → tray	mug, plate
52	apple → fruit plate	glass cup
53	orange → round plate	fork, square plate
54	spoon → plate	glass, fork, napkin
55	cup → tray	spoon, plate, bowl
56	cup → tray	napkin, plate
57	banana → plate	fork, orange, napkin
58	potato → basket	knife, onion, cutting board
59	tomato → bowl	spoon, potato, plate
60	black pen → round container	stapler, red pencil, notebook
61	cucumber → plate	knife, carrot, cutting board
62	blue cup → tray	spoon, plate
63	spoon → white plate	fork, glass
64	apple → fruit bowl	knife, plate
65	orange → green napkin	salt shaker, plate
66	banana → plate	fork, glass
67	lemon → metal bowl	knife, plate
68	tomato → white plate	fork, napkin
69	pear → basket	mug, plate
70	red marker → pen holder	mug, notebook
71	eraser → notebook	pen
72	green apple → tray	fork, plate
73	teacup → saucer	spoon, napkin
74	knife → wooden cutting board	spoon, plate
75	banana → basket	mug, plate
76	lemon → napkin	fork, plate
77	mushroom → saucepan	spoon, plate
78	potato → plate	fork, glass
79	yellow cup → basket	spoon, plate
80	apple → cutting board	knife, plate
81	spoon → saucer	cup, plate
82	spatula → plate	salt shaker, bowl
83	red block → blue box	lamp, book
84	banana → bowl	spoon, plate
85	pear → napkin	spoon, plate
86	red apple → wicker basket	mug, plate
87	green lime → white bowl	knife, plate
88	yellow banana → wooden cutting board	knife, bowl
89	strawberry → small saucer	fork, napkin
90	carrot → soup pot	knife, cutting board
91	soup spoon → empty bowl	plate, napkin
92	pepper grinder → metal tray	salt shaker, napkin
93	red marker → white mug	mouse, keyboard
94	eraser → open notebook	pen
95	glue stick → plastic bin	stapler, mouse pad
96	pencil sharpener → green tray	book
97	lego brick → plastic bucket	remote control, book
98	chess pawn → chessboard	mug, book
99	sponge → sink basin	towel

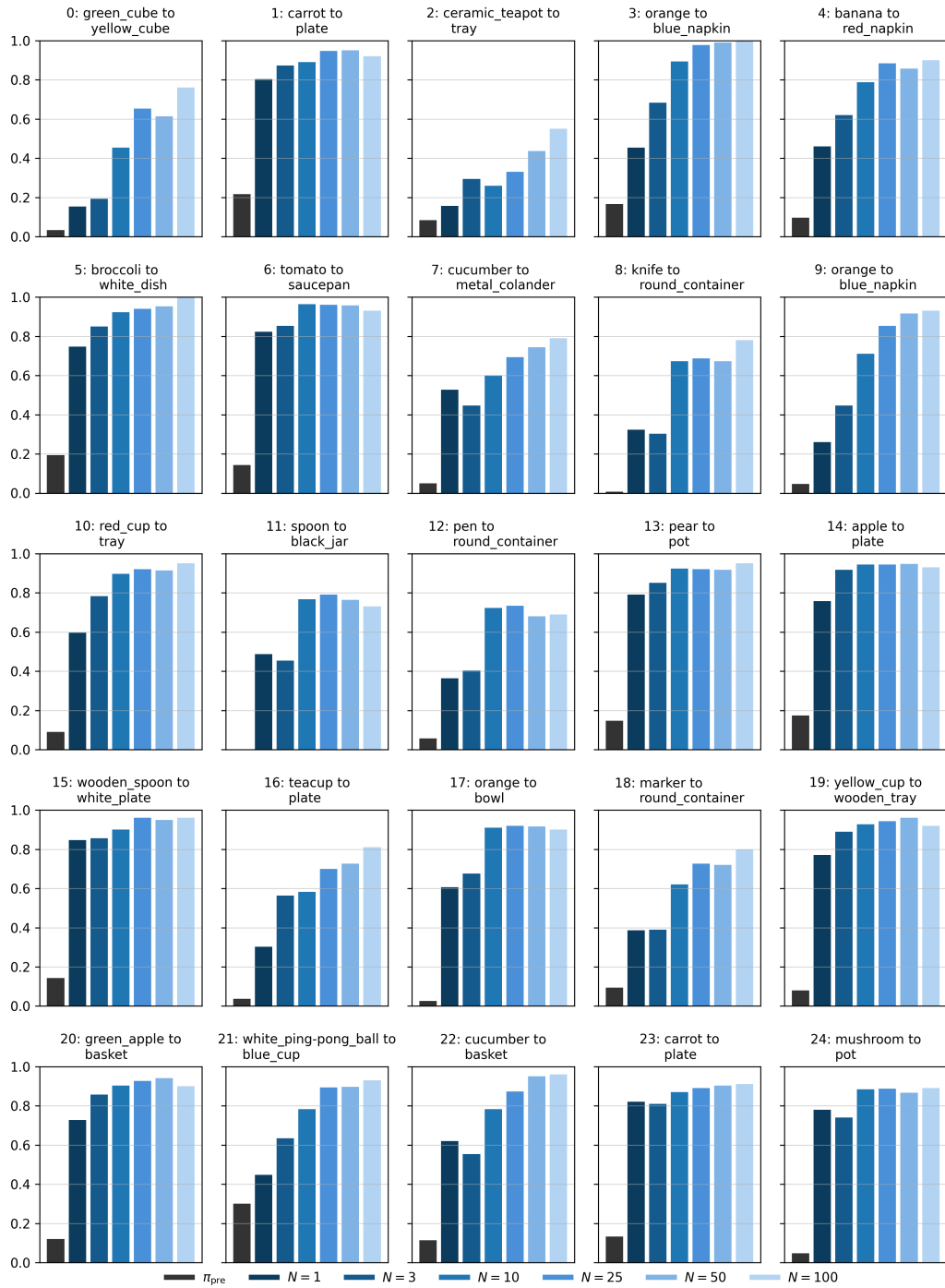


Figure F.4: Success rates for scenes 0-24.

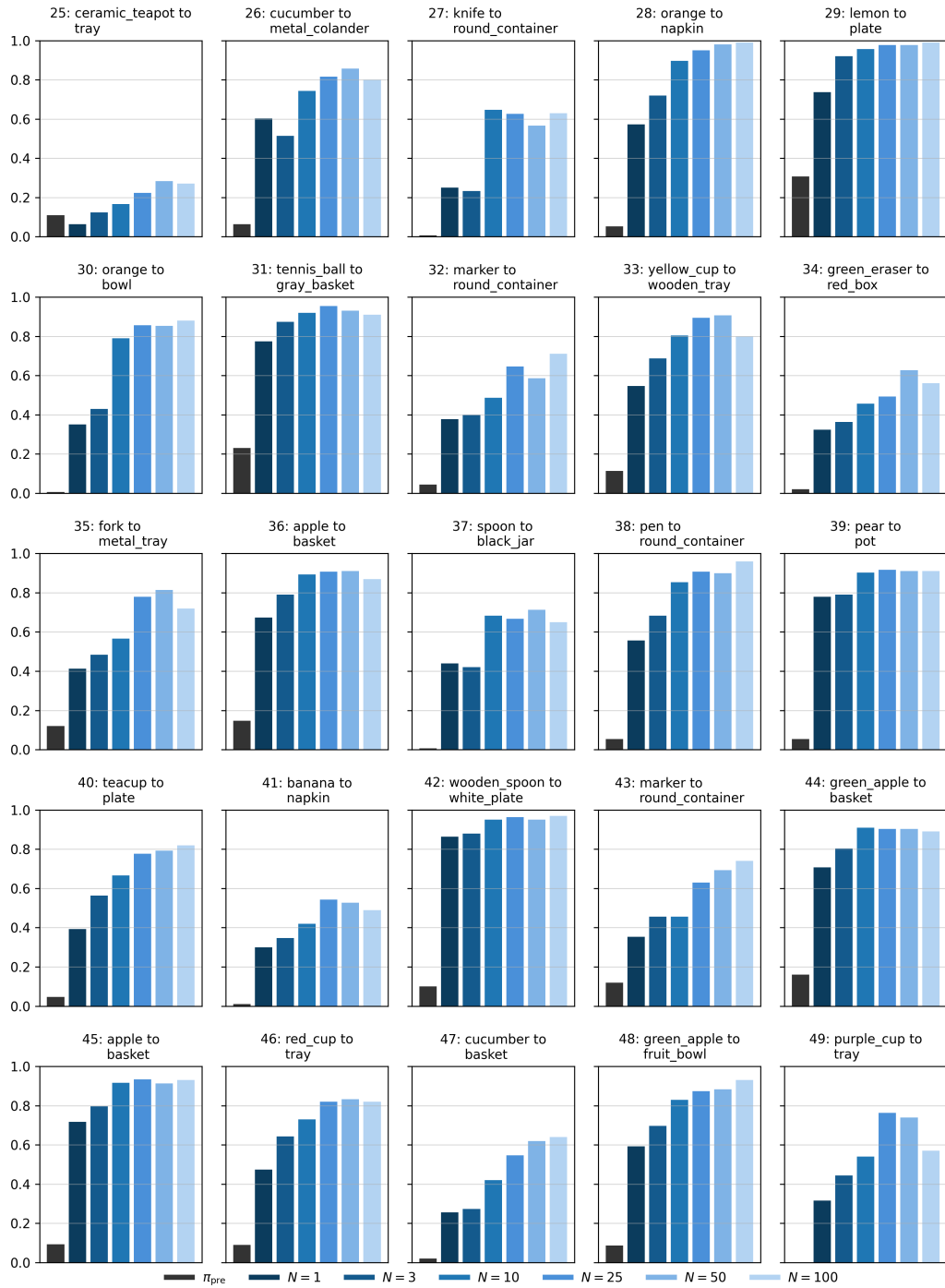


Figure F.5: Success rates for scenes 25-49.

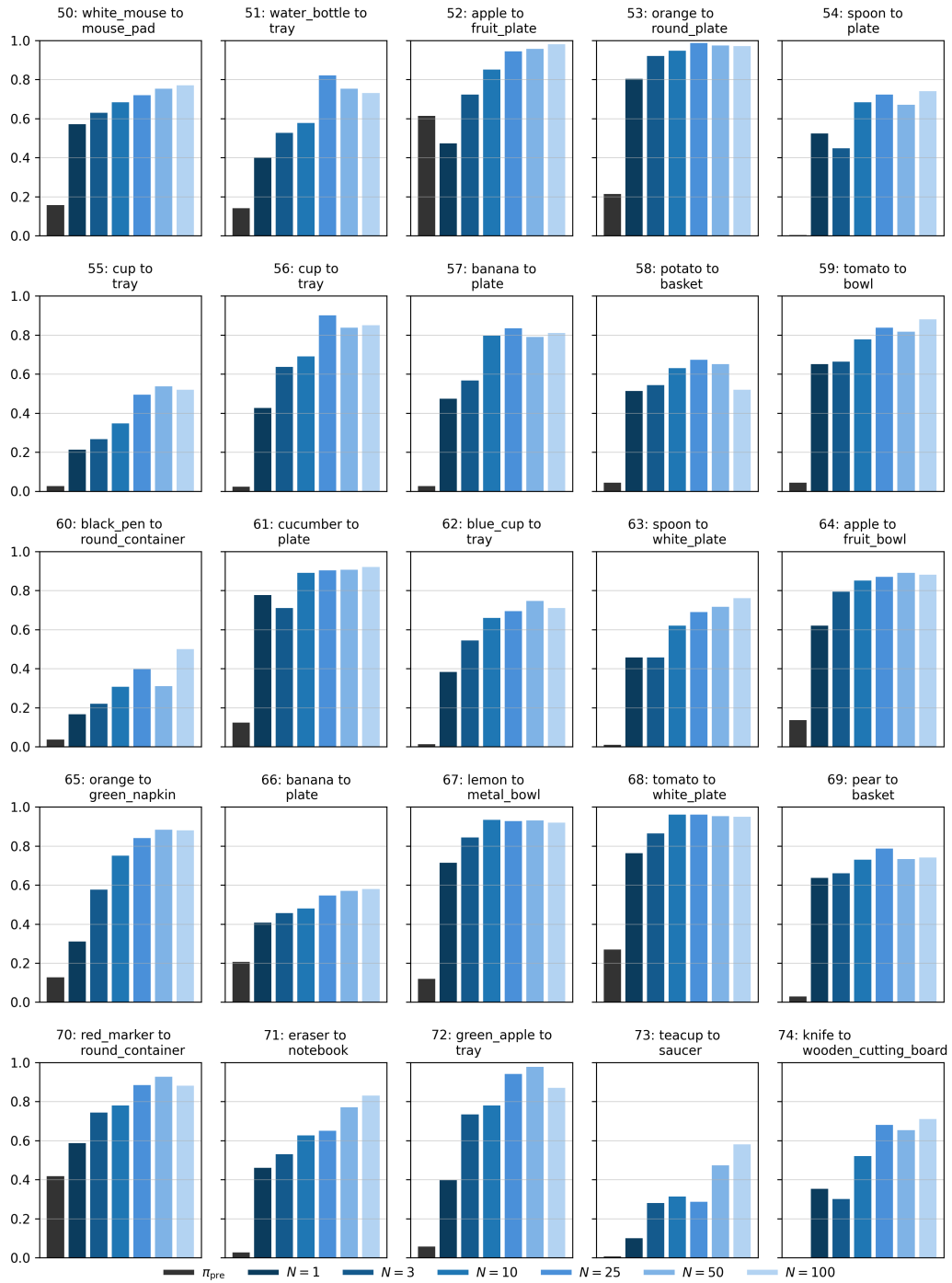


Figure F.6: Success rates for scenes 50-74.

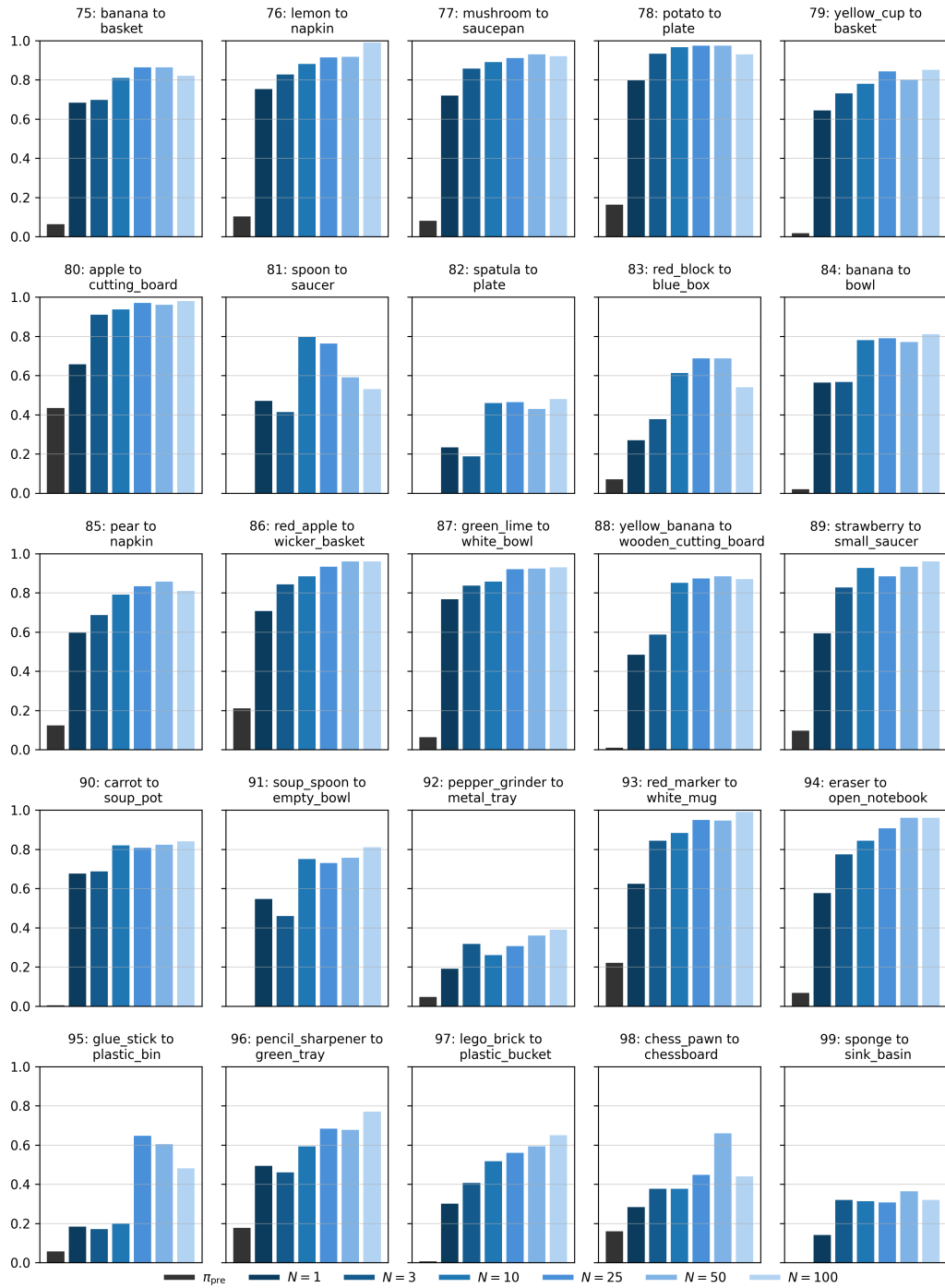


Figure F.7: Success rates for scenes 75-99.

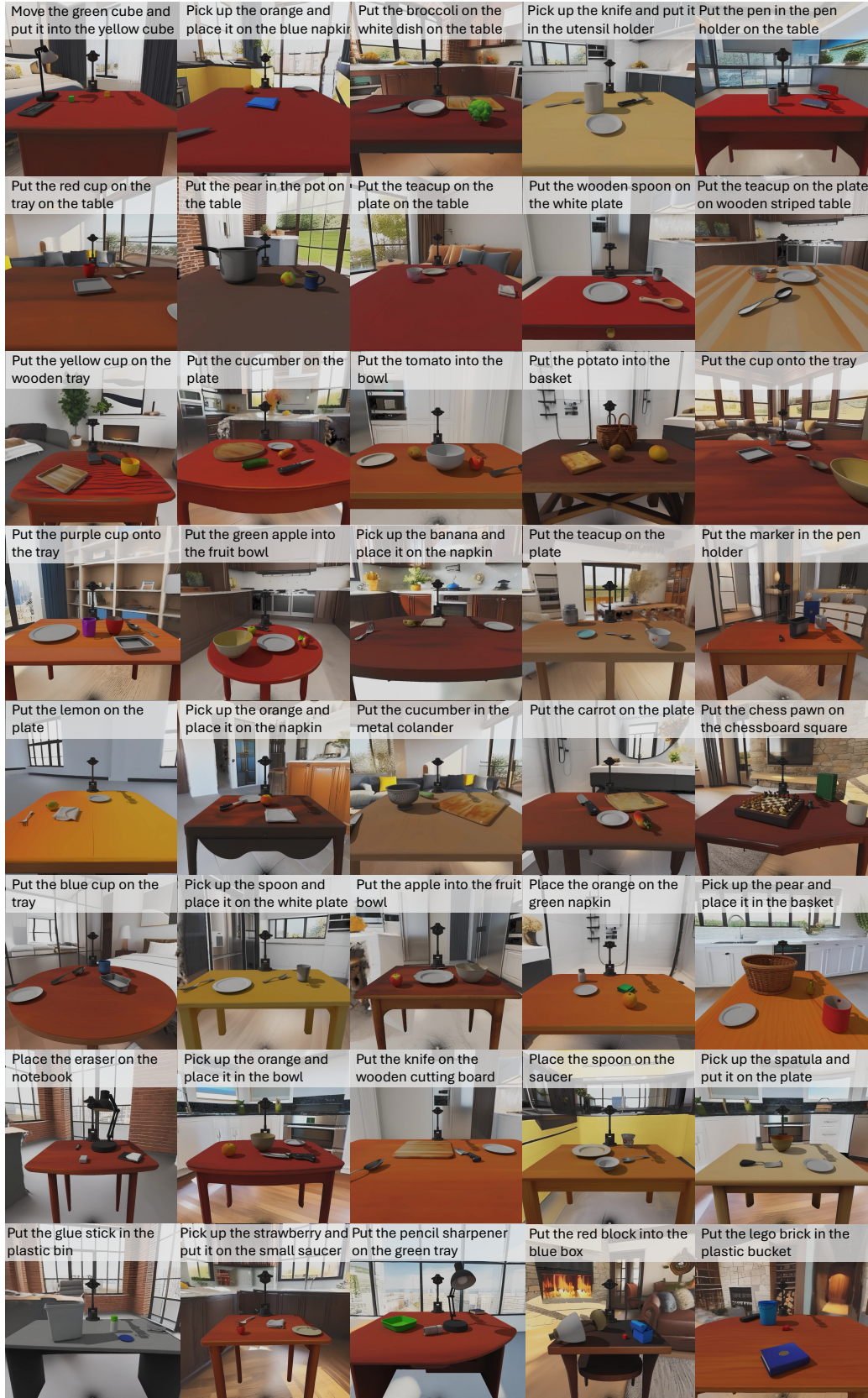


Figure F.8: Generated example simulation scenes for RL fine-tuning. Zoom in for details.

H Real-world Rollout Examples

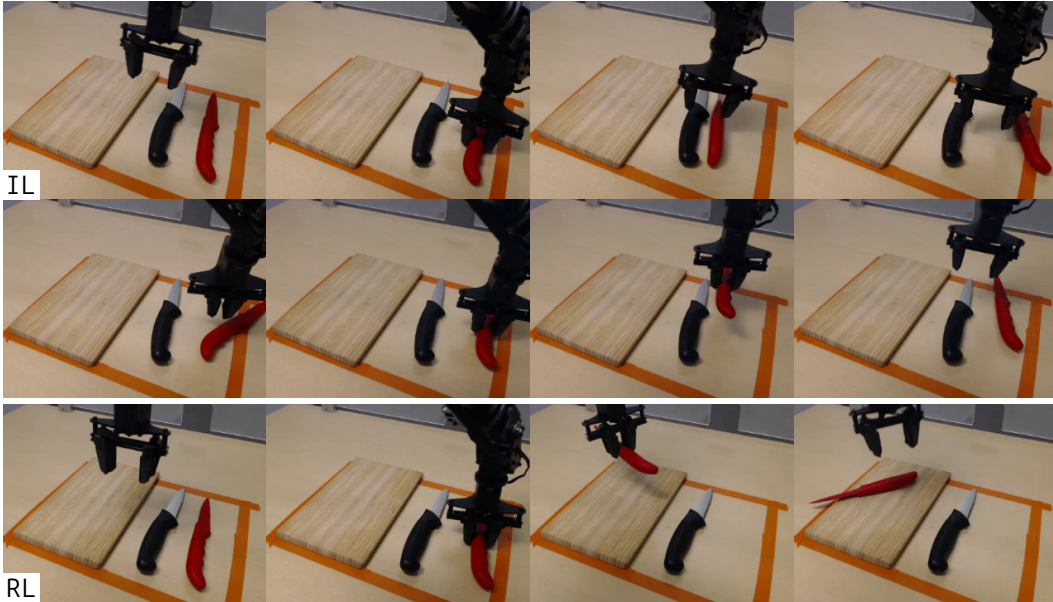


Figure H.11: **IL: semantic failure. RL: success.** A trial example of the red knife \rightarrow cutting board task (scene 7 from Table 2). The imitation learning (IL) policy first grasps the red knife but immediately drops it after entering an out-of-distribution state. It then grasps and lifts the knife once more before dropping it again and eventually timing out. In comparison, the reinforcement learning (RL) policy grasps the red knife and deliberately places it on the cutting board.

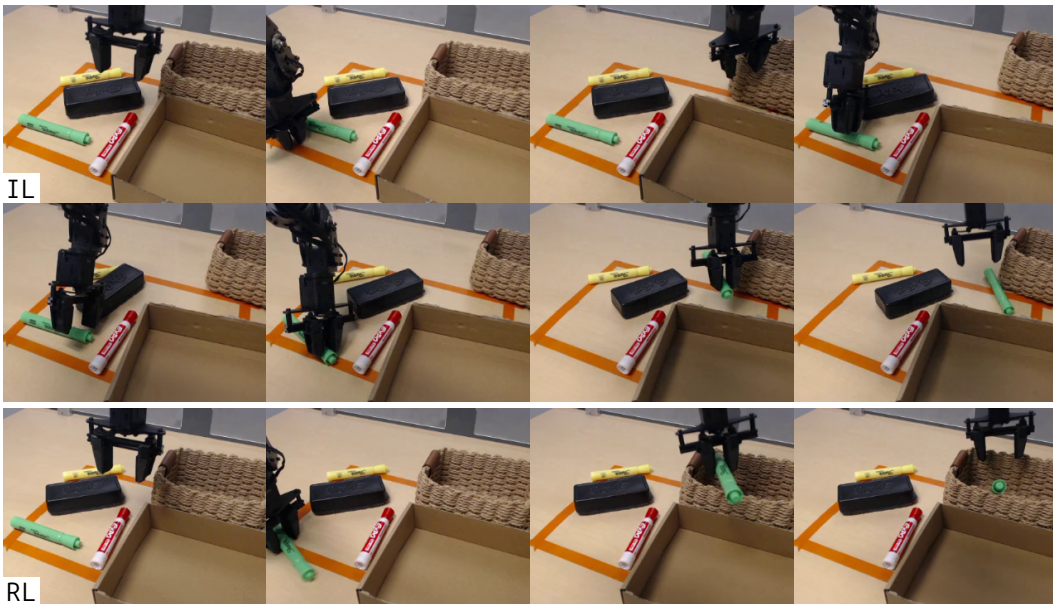


Figure H.12: **IL: dynamics failure. RL: success.** A trial example of the green marker \rightarrow basket task (scene 9 from Table 2). The IL policy initially misses the grasp on the green marker and then pushes the basket away. It makes two regrasp attempts before finally lifting the marker, but places it next to the basket instead of inside it and eventually times out. In comparison, the RL policy correctly places the green marker inside the basket.

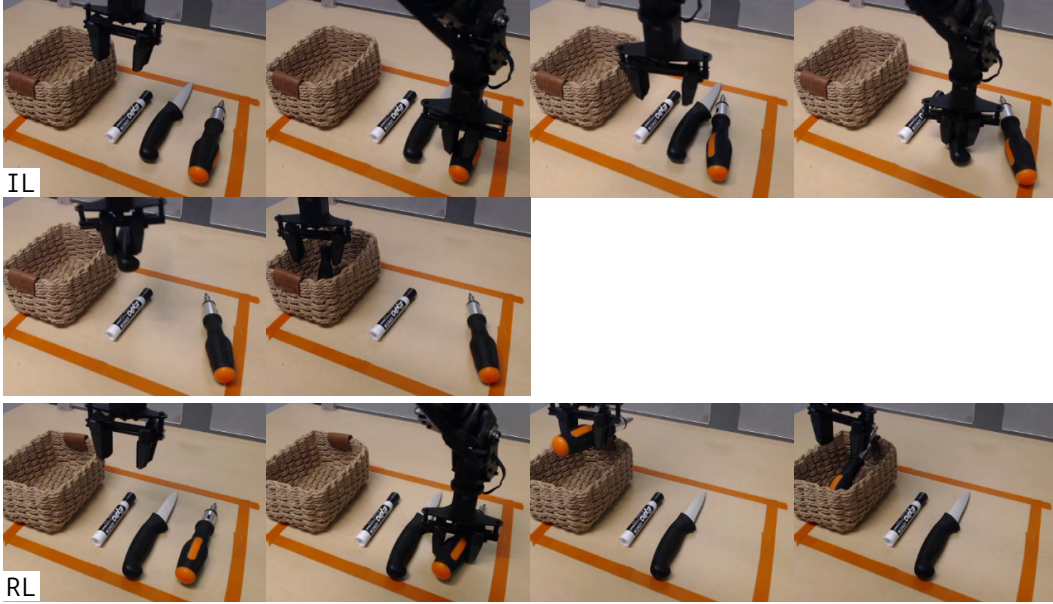


Figure H.13: **IL: dynamics and semantic failure. RL: success.** A trial example of the screwdriver \rightarrow basket task (scene 10 from Table 2). The IL policy attempts to grasp the screwdriver but misses. It then becomes confused and grasps the knife instead, placing it in the basket and failing due to incorrect task execution. In comparison, the RL policy correctly places the screwdriver in the basket.

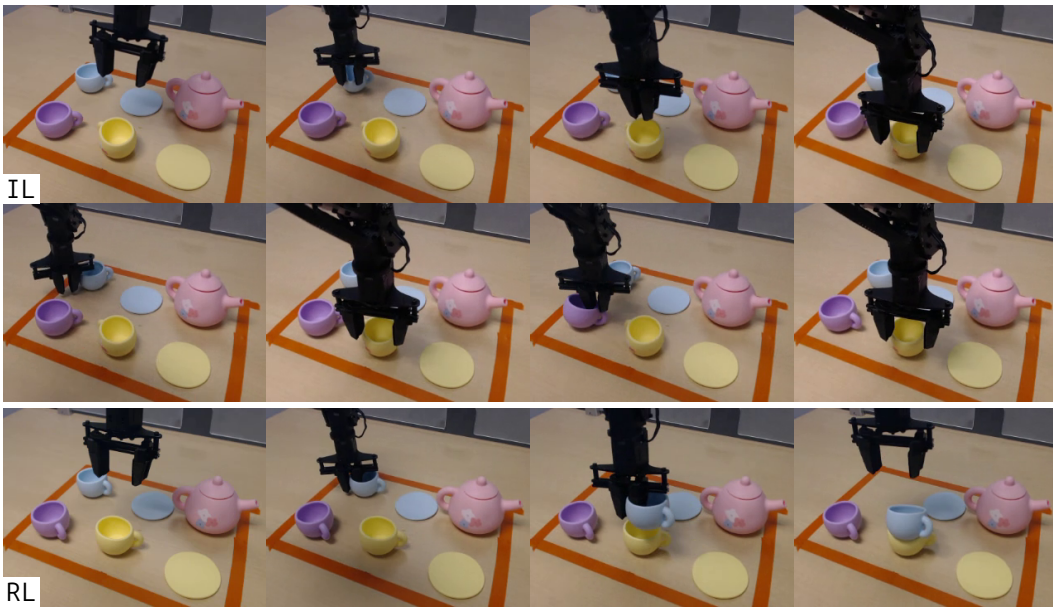


Figure H.14: **IL: dynamics and semantic failure. RL: success.** A trial example of the blue teacup \rightarrow yellow teacup stacking task (scene 11 from Table 2). The IL policy first misses the grasp on the blue teacup and then moves toward the yellow teacup twice. It subsequently becomes confused and attempts to grasp the purple teacup instead, eventually timing out. In comparison, the RL policy quickly grasps the correct teacup and stacks it onto the yellow one.

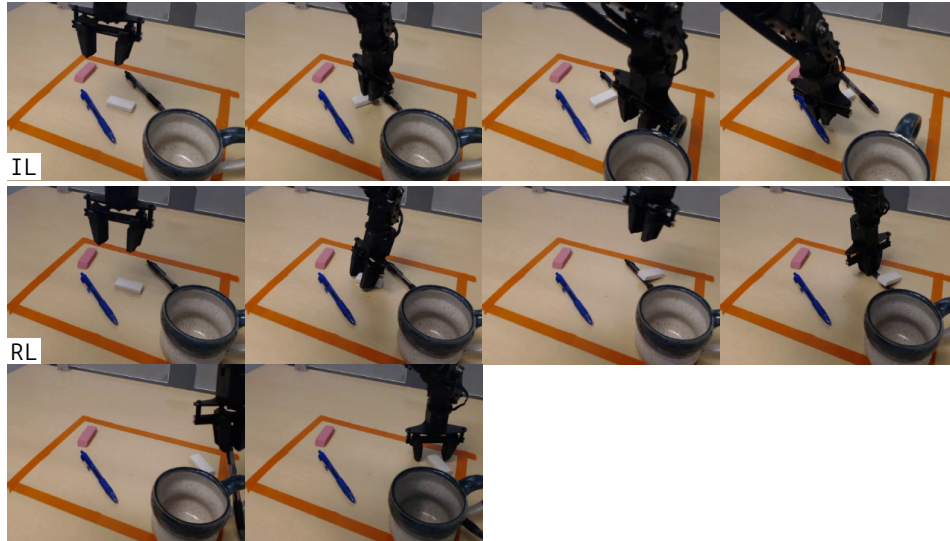


Figure H.15: **IL: dynamics failure. RL: dynamics failure.** A trial example of the white eraser \rightarrow mug task (scene 6 from Table 2). The IL policy misses the grasp on the white eraser several times before ultimately hovering, leading to a timeout. In contrast, the RL policy successfully grasps and lifts the white eraser, but it slips from the grasp and falls onto the black pen, confusing the policy. The policy then grasps and clears the black pen before returning to the white eraser, but still times out.

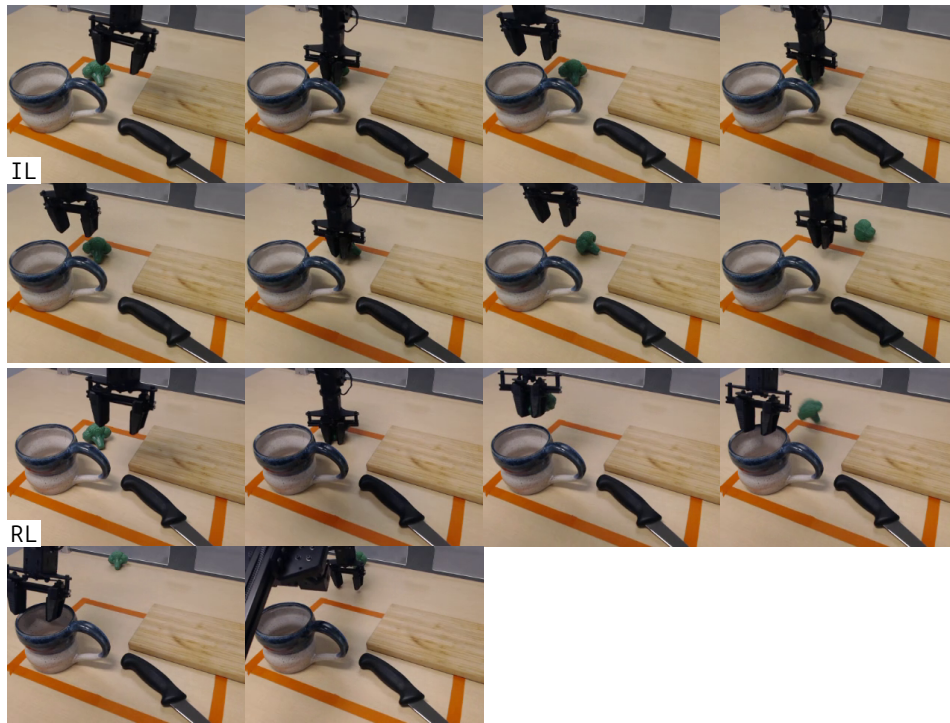


Figure H.16: **IL: dynamics failure. RL: dynamics failure.** A trial example of the broccoli \rightarrow mug task (scene 1 from Table 2). The IL policy repeatedly misses the grasp on the broccoli and eventually times out. In contrast, the RL policy quickly grasps the broccoli and attempts to place it into the mug, but it hits the edge and rolls out of reach of the manipulator. A significant portion of failures was caused by objects moving out of reach, preventing regrasp attempts.